

Bioinspired gel polymer electrolyte for wide temperature lithium metal battery

Received: 3 June 2024

Accepted: 5 March 2025

Published online: 12 March 2025



Shuohan Liu¹, Wensheng Tian², Jieqing Shen¹, Zhikai Wang¹, Hui Pan¹✉, Xuchen Kuang¹, Cheng Yang²✉, Shunwei Chen³, Xiujuan Han³✉, Hengdao Quan⁴ & Shenmin Zhu¹✉

Stable operation of Li metal batteries with gel polymer electrolytes in a wide temperature range is highly expected. However, insufficient dynamics of ion transport and unstable electrolyte-electrode interfaces at extreme temperatures greatly hinder their practical applications. We report a bioinspired gel polymer electrolyte that enables high-energy-density Li metal batteries to work stably in a wide temperature range from -30 to 80 °C. The wide-temperature gel polymer electrolyte is fabricated by using a branched polymer of which side chains are double coupled with their asymmetric analogues. The double dipole coupling regulates the Li^+ coordination environment to form a weak solvation structure that offers fast and uniform Li^+ deposition at extreme temperatures. Consequently, the non-flammable gel polymer electrolyte displays an ionic conductivity of $1.03 \times 10^{-4} \text{ S cm}^{-1}$ at -40 °C and a Li^+ transference number of 0.83. The Li metal batteries with $\text{LiNi}_{0.8}\text{Co}_{0.1}\text{Mn}_{0.1}\text{O}_2$ positive electrode deliver initial specific discharge capacities of 121.4 mAh g^{-1} at -30 °C and 172.2 mAh g^{-1} at 80 °C, with corresponding discharge currents of 18.8 mA g^{-1} and 188 mA g^{-1} , respectively. Additionally, a pouch cell delivers a specific energy up to 490.8 Wh kg^{-1} .

Operation temperature range is a vital factor for energy storage devices that affects human life. The operating temperatures of commercial lithium-ion batteries are generally in the range of -20 to 60 °C, and higher operation temperatures would cause terrible safety issues due to the low-boiling and flammable liquid electrolytes^{1,2}. Solid-state lithium batteries are hoped to offer high safety but usually suffer from poor low-temperature performance, especially below 0 °C^{3,4}. As an intermediate state between liquid electrolytes and solid polymer electrolytes, gel polymer electrolytes (GPEs) are considered among the most promising electrolytes for lithium-metal batteries due to their high ionic conductivity, great flexibility, and favorable electrode-electrolyte interfaces (EELs)^{5–7}. However, conventional GPEs typically show poor ion transport and high desolvation energy at low temperatures (LT, <25 °C), and intense side reactions at high temperatures (HT, >80 °C)^{8,9}.

To achieve a temperature-independent electrolyte, building weak solvation structures has been recognized as one of the most effective approaches, because both the ion transport behavior and desolvation energy are closely related to the Li^+ solvation structure^{10,11}. Moreover, the anions in weakened Li^+ solvation structure would preferentially decompose at the EELs to form an inorganic-rich passivation layer, which benefits Li^+ deposition^{12–14}. Current techniques to achieve weak solvation structures in GPEs mainly focus on the modulation of the liquid components^{15–18}. Few studies have attempted to construct a weakly solvated structure by regulating the polymer framework in GPEs.

Water grasses, commonly found in lakes and rivers, have evolved special structures to adapt to aquatic environments. The hydrophobic wax layer on their leaf surfaces has disappeared, enhancing interaction with water to capture nutrients. Their brush-like leaves increase the

¹State Key Laboratory of Metal Matrix Composites, School of Materials Science and Engineering, Shanghai Jiao Tong University, Shanghai, China. ²State Key Laboratory of Space Power-Sources, Shanghai Institute of Space Power-Sources, Shanghai, China. ³School of Materials Science and Engineering, Qilu University of Technology (Shandong Academy of Sciences), Jinan, Shandong, China. ⁴School of Chemistry and Chemical Engineering, Beijing Institute of Technology, Beijing, China. ✉e-mail: panhui115@sjtu.edu.cn; yangcheng_811@sina.com; xjhan@qlu.edu.cn; smzhu@sjtu.edu.cn

contact area with the water and can swing quickly, allowing water to pass through rapidly¹⁹. Inspired by the interaction between water grass and water, we propose that a weakly solvated structure in GPE can be achieved by regulating the interaction between the polymer framework and the encapsulated liquid components. Simultaneously, a brush-like polymer framework, similar to that of water grass, can provide more interaction sites^{20–22}.

Herein, we design a Li^+ solvation cluster to form unique dynamic non-bonding interactions with the short side chains of the brush polymer, mimicking the dynamic interactions of the water grass with water (Fig. 1a). Poly(trifluoroethyl methacrylate) (PTFMA) was selected as the brush-like polymer framework, and ethyl 3,3,3-trifluoropropanoate (FEP) that has an asymmetric structure towards the polymer side chains was used as the coupling agent. The double dipole coupling interaction between FEP and PTFMA enriches FEP around the polymer brushes and effectively reduces the coordination between FEP and Li^+ (Supplementary Fig. 1 and 1b). As results, the weakly solvated gel polymer electrolyte (WSGPE) displays ionic conductivity of 4.40×10^{-4} and $1.03 \times 10^{-4} \text{ S cm}^{-1}$ at 25°C and -40°C , respectively, with a Li^+ transference number of 0.83 and an electrochemical window of 5.05 V (Fig. 1c). In addition, WSGPE showed fire resistance ensuring the safety of high-voltage batteries (Fig. 1d). Consequently, the weak solvation structure formed in WSGPE enabled the Li metal batteries to operate over a wide temperature range (-30 – 80°C). In particular, the WSGPE can be used in high-voltage Li metal batteries, and a pouch cell with a specific energy of 490.8 Wh kg^{-1} was fabricated. This work presents a straightforward and practical method to the development of high-performance GPEs for wide temperature Li metal batteries.

Results

Materials design and solvation structure regulation

Trifluoroethyl methacrylate (TFMA) monomer was used for in situ polymerization to form a brush-like PTFMA framework, and FEP was

employed to act as a coupling agent, which formed unique dynamic non-bonding interactions with the short side chains of PTFMA. A tiny amount of fluoroethylene carbonate (FEC) was added to optimize the interface and poly(ethylene glycol) diacrylate (PEGDA) was used as a cross-linking agent. The transparent WSGPE was obtained by curing the precursor mixture at 70°C for 5 h (Supplementary Fig. 2). The disappearance of $\text{C}=\text{C}$ peak in Fourier transform infrared (FTIR) spectra suggests the successful polymerization occurred (Supplementary Fig. 3)^{23,24}.

The interactions between components were calculated by density functional theory (DFT) (Supplementary Data 1). Supplementary Table 1 shows that PTFMA and FEP have the strongest binding energy, which can be demonstrated indirectly by electrostatic potential (ESP). As shown in Fig. 2a, the oxygen atoms of $\text{C}=\text{O}$ dipole in PTFMA and FEP show the most negative potential. Due to the strong electron-withdrawing ability of $-\text{CF}_3$, the β -site carbon atoms of $-\text{CF}_3$ show the highest positive potential both in PTFMA and FEP. Therefore, the double dipole coupling bonds are formed between the FEP and side chains of PTFMA. Compared to single dipole coupling, double dipole coupling bonds are much stronger that FEP can be fixed to PTFMA to prevent leakage. More importantly, it is conducive to reorganizing the Li^+ coordination structure by expelling FEP out of the first Li^+ solvation sheath to form a weak solvation structure. The snapshot of the molecular dynamics (MD) simulation in Fig. 2b shows that PTFMA is surrounded by a large amount of FEP, in agreement with DFT results. The distribution of other components also confirms the priority enrichment of FEP around PTFMA (Fig. 2c). An additional experiment has been carried out to further demonstrate that the double dipole coupling interaction is unique between the FEP and PTFMA (Supplementary Fig. 4). The TFMA was polymerized firstly to obtain the linear PTFMA, and then equal amounts of FEP and FEC solvents were added, respectively, denoted as PTFMA + FEP and PTFMA + FEC, correspondingly. For PTFMA + FEP, after curing at RT for 8 h, a transparent homogeneous bulk in solid-like state was obtained without fluidity. By

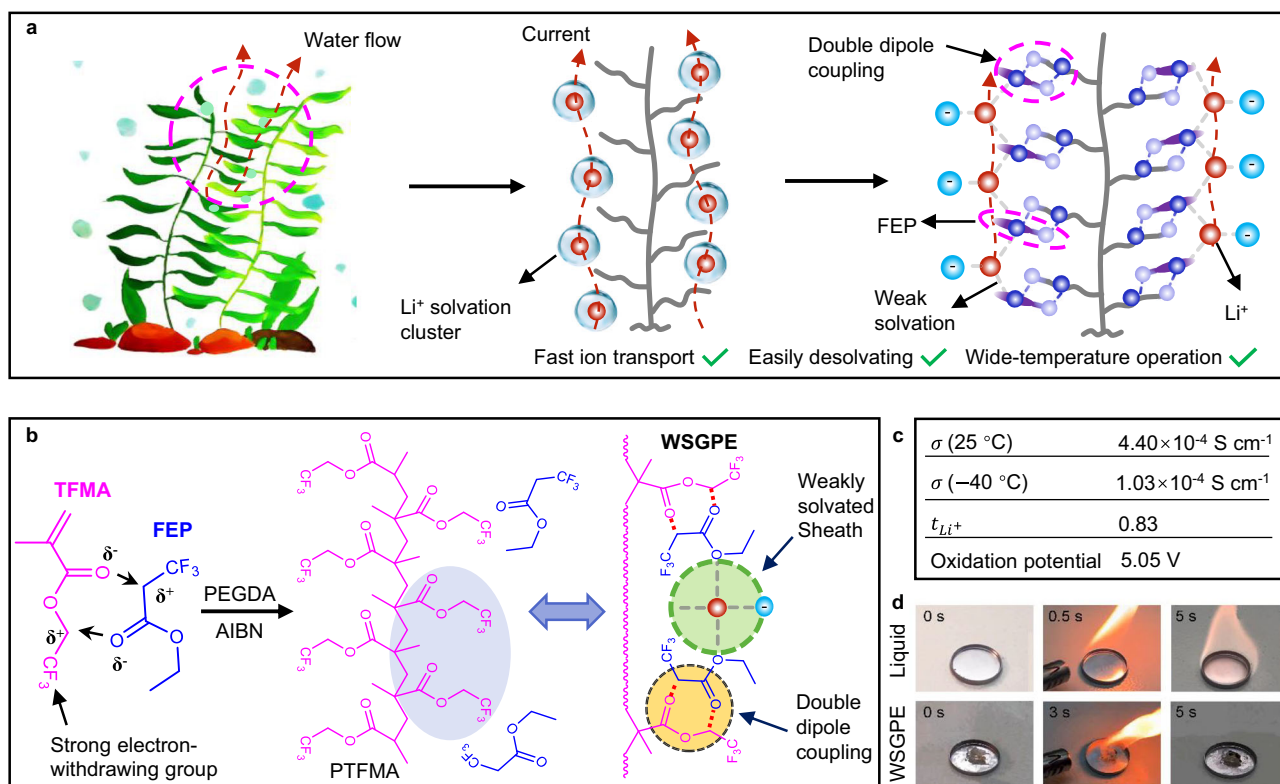


Fig. 1 | Material design, fabrication, and properties of bioinspired WSGPE. a Bioinspired WSGPE. **b** Structures and fabrication method of WSGPE. **c** Electrochemical properties of WSGPE. **d** Flame-retardant performance of WSGPE. Source data are provided as a Source Data file.

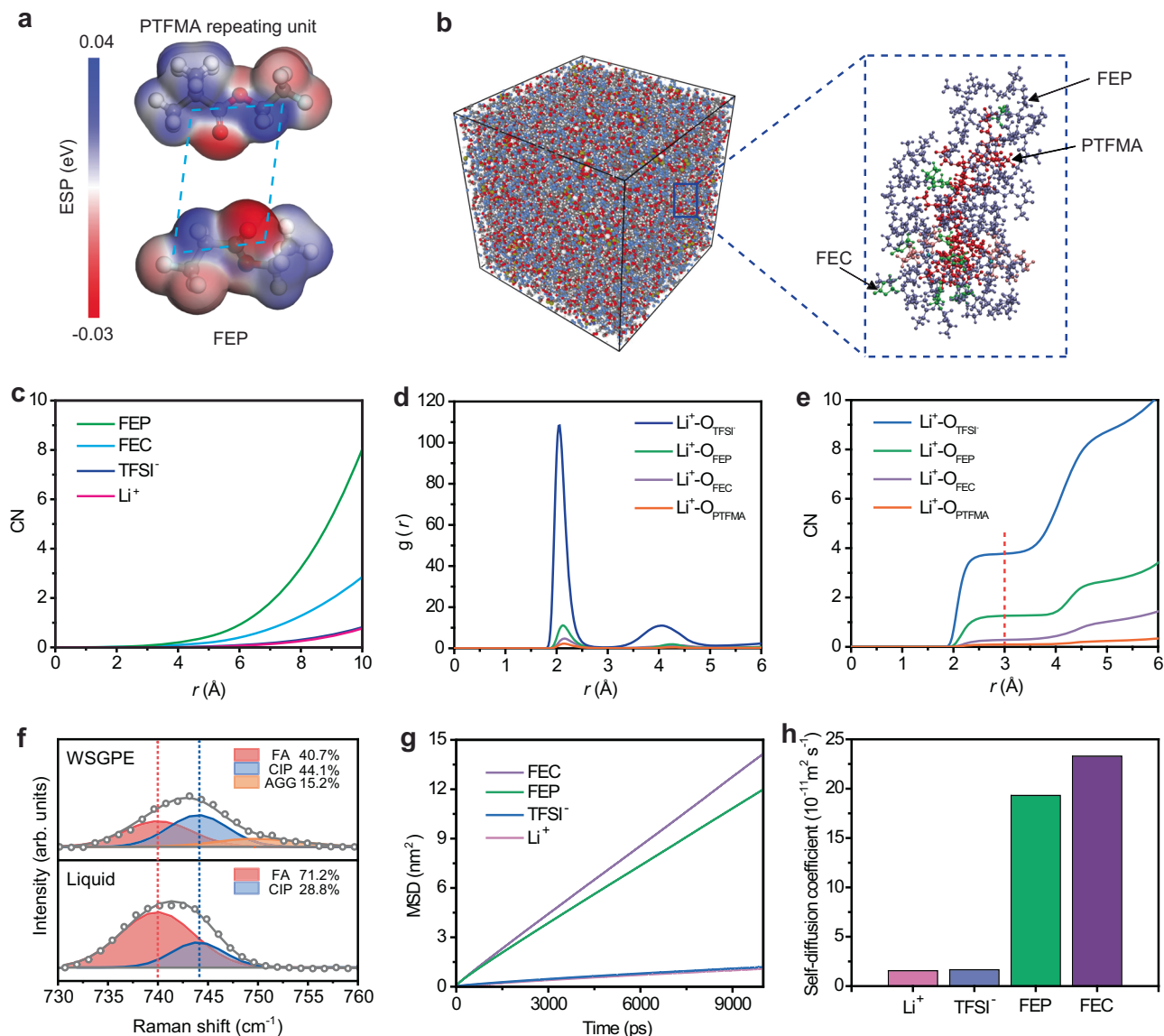


Fig. 2 | Solvation structure of WSGPE. a ESP of PTFMA repeating unit and FEP (Color code: gray, C; pale blue, F; red, O; white, H). **b** Snapshots of the WSGPE MD simulation. **c** CNs of PTFMA. RDFs (**d**) and CNs (**e**) of Li⁺ in WSGPE. **f** Raman spectra

of liquid electrolyte and WSGPE. MSD-time curves (**g**) and the corresponding diffusion coefficients (**h**) of WSGPE components. Source data are provided as a Source Data file.

contrast, there is still a clear solid-liquid interface between FEC and PTFMA for PTFMA + FEC. These results suggest that there is a strong interaction between PTFMA and FEP, leading to a solid-like state at RT.

The solvation structure and ion transport behavior of Li⁺ in WSGPE and liquid electrolyte (1M LiTFSI in FEP with 5 wt% FEC) were analyzed by MD simulations (Supplementary Data 2 and 3). The radial distribution function (RDF) and the corresponding coordination number (CN) in the WSGPE are shown in Fig. 2d, e. In Fig. 2d, the initial peak corresponding to the Li⁺-O (TFSI⁻) appears at 2.06 Å, which is much shorter than that of Li⁺-O (FEP) (2.12 Å) and Li⁺-O (FEC) (2.16 Å). Comparing the CNs at the distance of 3.0 Å, they are 1.30, 0.31, 3.71, and 0.08 for FEP, FEC, TFSI⁻ and PTFMA, respectively. These results suggest that the first Li⁺ solvation sheath in WSGPE is anion-rich and the obtained solvation structure is similar to those local high-concentration electrolytes (LHCEs)^{25,26}. In contrast, the first Li⁺ solvation sheath in liquid electrolyte is dominated by the FEP solvent (CNs of FEP, FEC and TFSI⁻ at 3 Å are 2.85, 0.59 and 1.96, respectively) (Supplementary Fig. 5). The solvation structure was further revealed by Raman spectroscopy (Fig. 2f). The S–N–S stretching vibration of

TFSI⁻ is usually composed of three components: free anions (FAs, uncoordinated TFSI⁻) at 740 cm⁻¹, contact ion pairs (CIPs, one TFSI⁻ coordinating to one Li⁺) at 744 cm⁻¹, and ion aggregates (AGGs, one TFSI⁻ coordinating to several Li⁺) at 749 cm⁻¹²⁷. Through peak integration, the contents of FAs, CIPs and AGGs in WSGPE are 40.7%, 44.1% and 15.2%, respectively. The presence of a large number of CIPs minimizes solvent polarization and keeps the FEP away from the electrode to prevent side reactions²⁸. Also, this solvation structure can reduce the desolvation energy of Li⁺ thus to improve the LT performance of WSGPE²⁹. In contrast, the liquid electrolyte forms a solvation structure containing FAs (71.2%) and CIPs (28.8%) and no AGGs. More evidence can be found in the nuclear magnetic resonance (NMR) spectroscopy (Supplementary Fig. 6). Compared to the liquid electrolyte, the downfield shift of the ⁷Li NMR peak in WSGPE supports the formation of a weakened coordination environment of Li⁺. These results further demonstrate that the double dipole coupling effect facilitates the formation of weak solvation structure in WSGPE.

To substantiate this effect, two additional samples were prepared. We replaced FEP in WSGPE with an equal amount of FEC to obtain a

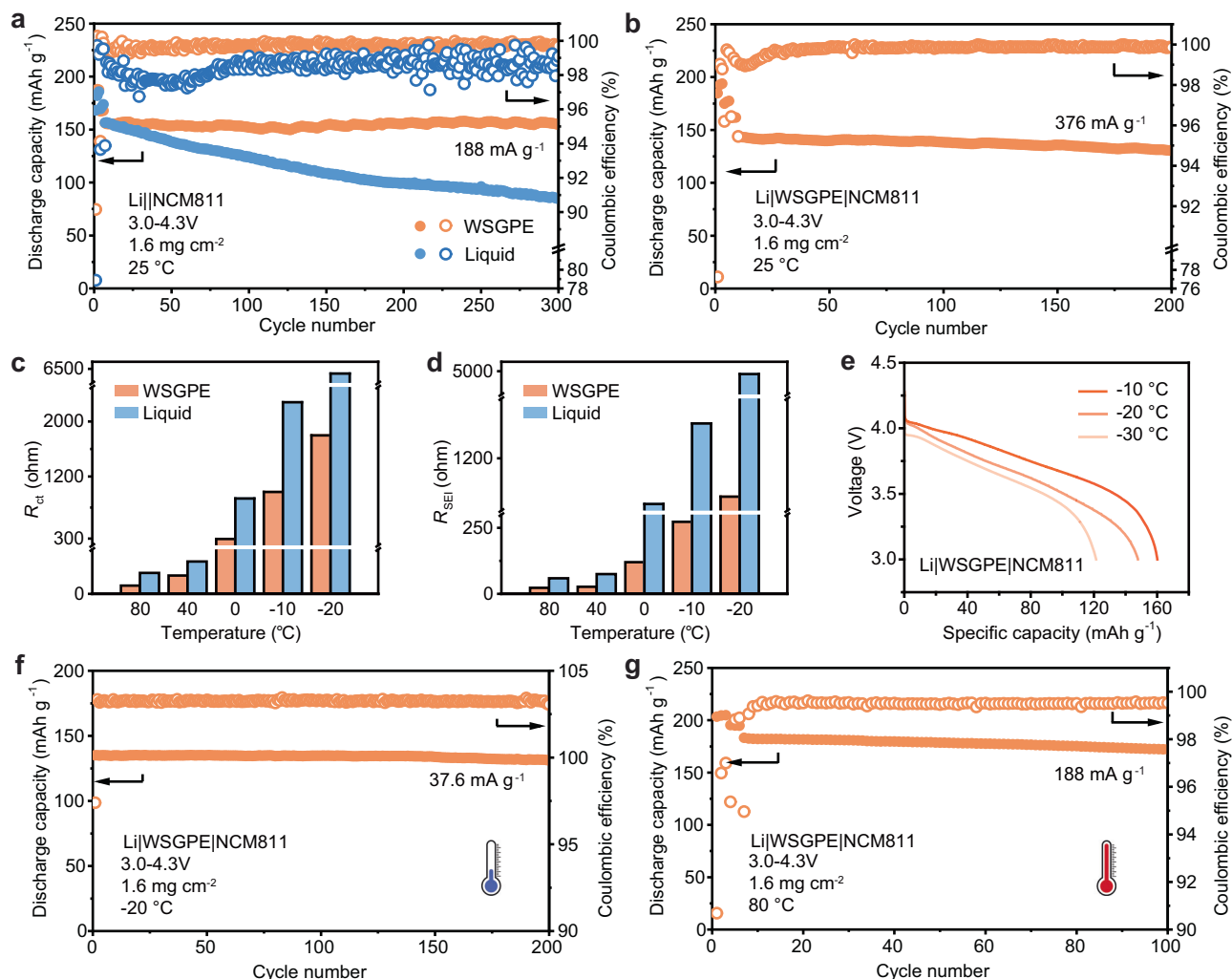


Fig. 3 | Electrochemical performance of Li||NCM811 cells. Cycling performance at 188 mA g⁻¹ (a) and 376 mA g⁻¹ (b), respectively. Comparison of R_{ct} (c) and R_{sei} (d) of the cells after 10 cycles at 188 mA g⁻¹ under different temperatures. e Discharge

curves of Li||WSGPE|NCM811 for the first cycle under 18.8 mA g⁻¹ at different temperatures. Cycling performance of Li||WSGPE|NCM811 cells at -20 °C (f) and 80 °C (g). Source data are provided as a Source Data file.

FEP-free gel polymer electrolyte (denoted as FEP-free GPE). Another one, namely PTFMA-free gel polymer electrolyte (denoted as PTFMA-free GPE), was prepared by replacing TFMA in the WSGPE precursor with an equal amount of PEGDA. The results from the analysis of FTIR and NMR indicate that the mirrored structure of PTFMA and FEP can effectively promote the generation of a weak solvation structure dominated by anions (Supplementary Figs. 7–9 and Supplementary Note 1).

Diffusion coefficients for the individual species in the WSGPE were calculated by fitting a time-dependent mean-square displacement (MSD) curve through the Einstein equation (Fig. 2g). The diffusion coefficients of Li⁺, TFSI⁻ and FEP are 1.56×10^{-11} , 1.66×10^{-11} and 1.93×10^{-10} m² s⁻¹, respectively (Fig. 2h). The diffusion coefficient of FEP is an order of magnitude higher than those of ions. According to the DFT results, it can be deduced that the FEP is accumulated around the polymer framework and transits rapidly. Therefore, the double dipole coupling bonds in WSGPE induce the formation of a weak solvation structure, which is crucial for rapid charge transfer at interfaces and the construction of stable EELs. Meanwhile, the fluorinated side chains can increase the electrochemical window efficiently³⁰.

Electrochemical performance of WSGPE

The WSGPE displays good electrochemical properties, including an electrochemical window of up to 5.05 V (Supplementary Fig. 10), a Li⁺

transference number of 0.83 (Supplementary Fig. 11) and an ionic conductivity of 4.40×10^{-4} S cm⁻¹ at RT (Supplementary Fig. 12). The wide electrochemical window, high ionic conductivity, and high Li⁺ transference number make WSGPE suitable for use in high-voltage Li metal batteries. Li||LiNi_{0.8}Co_{0.1}Mn_{0.1}O₂ (NCM811) cells were assembled with the WSGPE. As shown in Fig. 3a, the Li||WSGPE|NCM811 cell (mass loading 1.6 mg cm⁻²) delivers a capacity of 154.8 mAh g⁻¹ with a retention of 92.5% after 300 cycles (188 mA g⁻¹, 3–4.3 V). In contrast, the capacity of Li||NCM811 cell using liquid electrolyte is only 85.0 mAh g⁻¹, and only 50.1% of the initial capacity is retained. The Li||WSGPE|NCM811 cell exhibits promising cycling performance at a specific current of 376 mA g⁻¹, with a capacity of 130.4 mAh g⁻¹ after 200 cycles and a retention of 90.8%, as shown in Fig. 3b. Even under high cut-off voltage of 4.5 V, the Li||WSGPE|NCM811 cell still delivers a capacity of 120.8 mAh g⁻¹ at 188 mA g⁻¹ after 300 cycles, which shows a more satisfactory cycling stability than other electrolytes (Supplementary Fig. 13 and Supplementary Note 2). In addition, the Li||WSGPE|NCM811 cell also shows good rate and cycling performance when the mass loading of positive electrode is up to 3 mg cm⁻² (Supplementary Figs. 14 and 15). Further increasing the mass loading to 7 mg cm⁻², the Li||WSGPE|NCM811 cell is still able to deliver a capacity of 168.9 mAh g⁻¹ after 50 cycles at 18.8 mA g⁻¹ with no obvious capacity fading (Supplementary Fig. 16). The WSGPE is also suitable for a high-voltage LiCoO₂ (LCO) positive electrode. Li||WSGPE|LCO cells exhibit

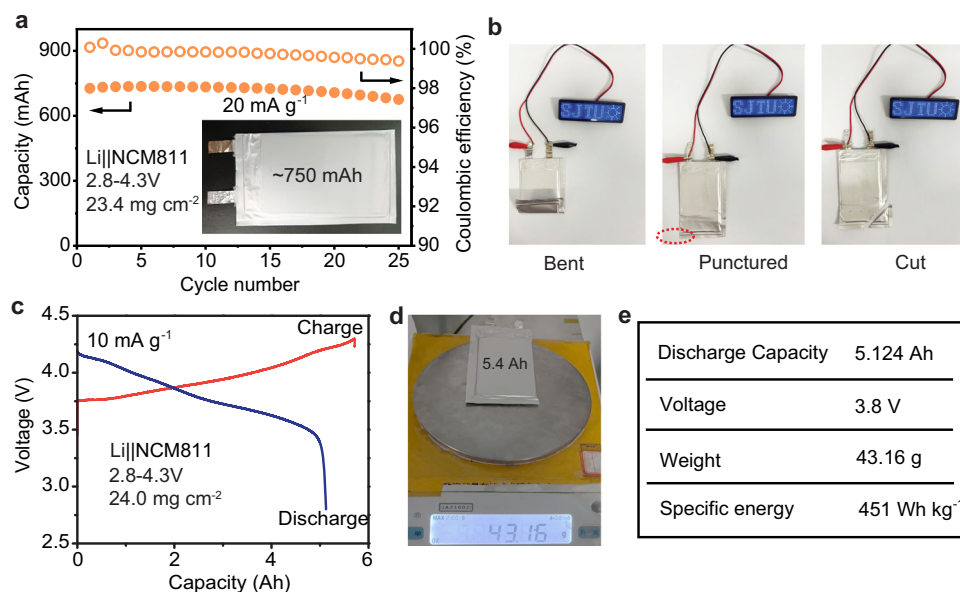


Fig. 4 | WSGPE based pouch cells. **a** Cycling performance of a pouch cell with designed capacity of 750 mAh at RT. **b** Combustion tests for pouch cell under bent, punctured and cut states. **c** Charge-discharge curves of a pouch cell with designed

capacity of 5.4 Ah at RT. **d** Image of weighting the pouch cell. **e** Specific energy calculation. Source data are provided as a Source Data file.

good rate and cycling performance in the voltage window of 3–4.6 V, with discharge capacities of 148.8 mAh g⁻¹ (150 cycles, 220 mA g⁻¹) and 106.6 mAh g⁻¹ (250 cycles, 440 mA g⁻¹), respectively (Supplementary Figs. 17–19).

The role of double dipole coupling bonds for interfacial charge transfer and EEIs formation was revealed by electrochemical impedance spectra (EIS) analysis. The variation of interfacial impedance along with cycling for Li||NCM811 cells (3–4.5 V) using different electrolytes is shown in Supplementary Fig. 20. The interfacial impedance of the Li|WSGPE|NCM811 cell is increased and then decreased rapidly and stabilized, which indicates that the interfacial layer generated by WSGPE has a high ionic conductivity and densifies rapidly with cycling (Supplementary Fig. 20a). Conversely, the interfacial impedance of liquid batteries is increased continuously with cycling (Supplementary Fig. 20b), caused by the constant fragmentation of the unstable interfacial layer and the unceasing decomposition of the electrolyte. Similar phenomenon is observed both in FEP-free GPE and PTFMA-free GPE batteries (Supplementary Fig. 20c, d). These suggest that all the control samples (liquid electrolytes, FEP-free GPE and PTFMA-free GPE) are unable to generate stable interfacial layers. Instead, WSGPE can form a stable interfacial layer during cycling, thus bringing in good cycling performance to high-voltage Li metal batteries.

The EIS of the WSGPE cell at different temperatures are shown in Supplementary Figs. 21 and 22 with the liquid cell as a comparison. Based on the equivalent circuit diagram of EIS for Li||NCM811 cells (Supplementary Fig. 23), the corresponding impedance values are summarized in Supplementary Table 2. Generally, both charge transfer resistance (R_{ct}) and solid electrolyte interphase (SEI) resistance (R_{SEI}) exhibit a significant temperature dependence^{31,32}. The WSGPE has a lower R_{ct} than liquid electrolyte at LT from -20 to 0 °C (Fig. 3c), suggesting the faster charge transfer at EEIs in Li||NCM811 cells using WSGPE. In addition, a significant decrease in R_{SEI} at both LT and HT is identified (Fig. 3d). Unlike the liquid batteries, the R_{SEI} in the WSGPE-based cells varies slightly with much smaller values, implying that the EEIs derived from the WSGPE are highly conductive for wide-temperature operation³³. The exchange current density (j_0) extracted from Tafel plots was used to quantitatively study interfacial Li⁺ transfer kinetics at -20 °C (Supplementary Fig. 24). The j_0 in WSGPE

(0.38 mA cm⁻²) is markedly larger than those in liquid electrolyte (0.29 mA cm⁻²), PTFMA-free GPE (0.21 mA cm⁻²) and FEP-free GPE (0.16 mA cm⁻²), implying fast interfacial Li⁺ transfer kinetics and the construction of highly conductive SEIs in WSGPE at LT.

Benefiting from the fast charge transfer at interfaces and satisfactory EEIs induced by the weak solvation structure, WSGPE exhibits good HT and LT performances that enables Li|WSGPE|NCM811 cells to operate in a wide temperature range (-30–80 °C). As shown in Supplementary Fig. 25, the WSGPE has a high ionic conductivity of 1.03×10^{-4} S cm⁻¹ at -40 °C. The Li|WSGPE|NCM811 cell delivers discharge capacities of 160.1, 147.9 and 121.4 mAh g⁻¹ at -10 °C, -20 °C and -30 °C, respectively (Fig. 3e). A high capacity of 131.2 mAh g⁻¹ with a capacity retention of 97.1% is obtained after 200 cycles at 37.6 mA g⁻¹ and -20 °C (Fig. 3f). Even at a specific current of 94 mA g⁻¹, a capacity retention of 95.5% (109.1 mAh g⁻¹) is observed after 200 cycles (Supplementary Fig. 26). Notably, WSGPE suppresses the performance deterioration of NCM811 at HT. After 100 cycles at 80 °C, the Li|WSGPE|NCM811 cell still delivers a capacity of 172.2 mAh g⁻¹ with a retention of 94.0% at 188 mA g⁻¹ (Fig. 3g).

To test the potential application of WSGPE, the self-discharge performance of Li||NCM811 cells were evaluated. A fully-charged WSGPE cell maintains a stable voltage (~4.2 V) even after storage for 15 days. However, the voltage of a fully-charged liquid cell rapidly decays from 4.3 V to below 4 V (Supplementary Fig. 27a). The cycling performance of the WSGPE cell after self-discharge storage is shown in Supplementary Fig. 27b. Due to the continuous decomposition of the liquid electrolyte, the liquid cell only delivers an initial capacity of 90.2 mAh g⁻¹, only 60% of that of WSGPE cell. These results suggest that self-discharge as well as the corrosion of Li metal batteries is effectively suppressed.

Pouch cells were assembled to check the availability of WSGPE for high-energy-density battery. As shown in Fig. 4a, a Li|WSGPE|NCM811 pouch cell with a designed capacity of 750 mAh was assembled (double-side coated positive electrode with mass loading of 23.4 mg cm⁻²; negative electrode: Li foil with thickness of 50 μm; N/P = 2.9). The voltage-capacity curves show that the as-assembled pouch cell has an average discharge voltage of 3.9 V and a practical discharge capacity of 726.8 mAh (Supplementary Fig. 28), corresponding to a specific energy of 490.8 Wh kg⁻¹ (Supplementary Table 3), irrespective of packaging

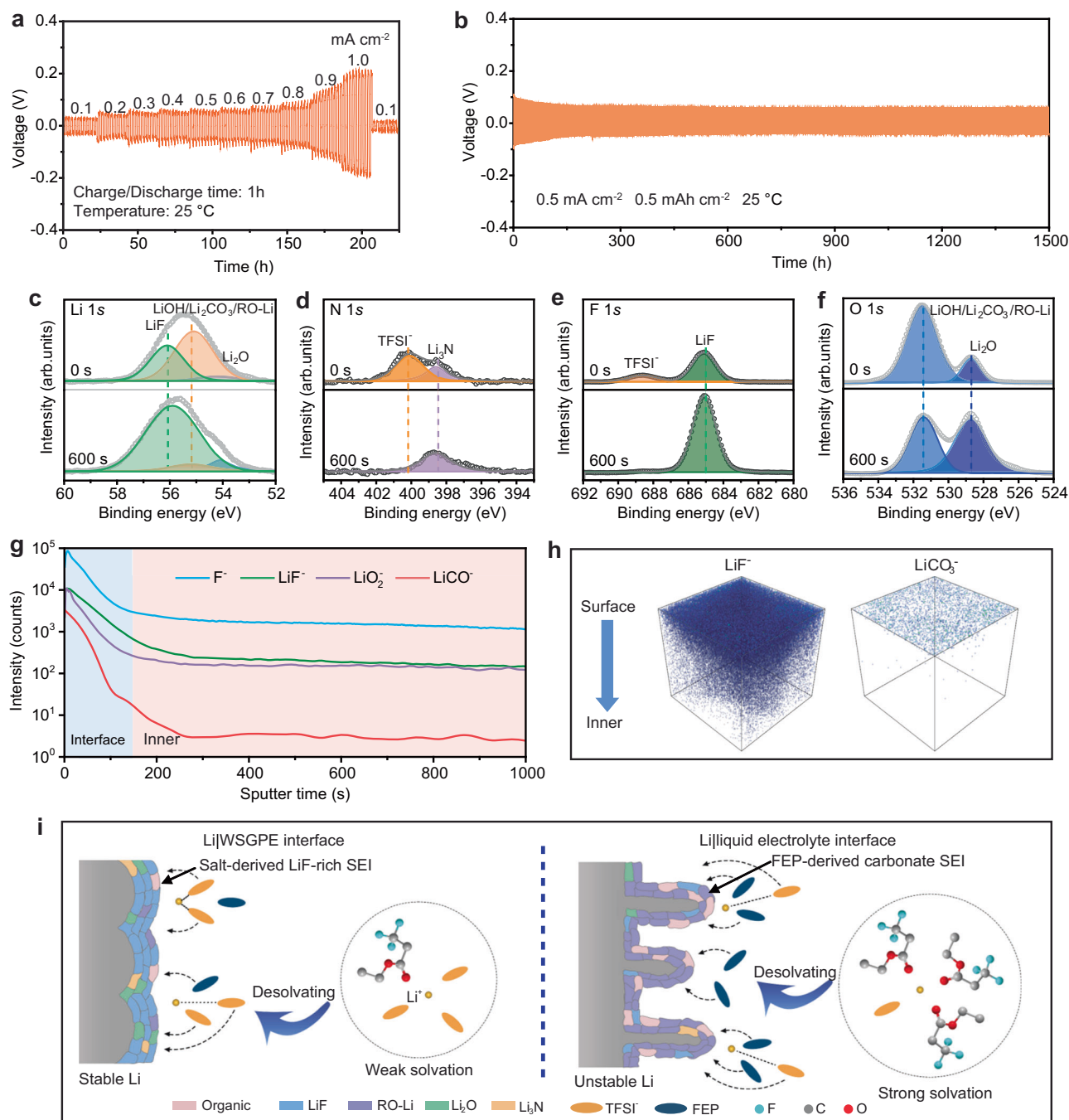


Fig. 5 | Li-WSGPE interface stability. Galvanostatic cycling curves of Li|WSGPE|Li cells under increasing current densities (**a**) and 0.5 mA cm⁻² (**b**). **c–f** XPS spectra of Li after 100 cycles in a Li symmetric cell at a current density of 0.5 mA cm⁻² and an area capacity of 0.5 mAh cm⁻². Li 1s (**c**), N 1s (**d**), F 1s (**e**) and O 1s (**f**). TOF-SIMS

depth profiles (**g**) and 3D view of fragments (LiF⁻ and LiCO₃⁻) distribution (**h**) of cycled Li (100 cycles at 0.5 mA cm⁻² and 0.5 mAh cm⁻²). **i** Schematic illustration of Li-electrolyte interface of Li|WSGPE|Li and Li|liquid electrolyte|Li batteries. Source data are provided as a Source Data file.

materials. The WSGPE has good nonflammability (Fig. 1d), which is important for improving the safety of high-nickel positive electrode batteries, especially under high-voltage operating conditions^{34,35}. As shown in Fig. 4b, the pouch cell can power an LED board even under a series of abusive conditions, including being bent, punctured, and cut, with no safety issues observed. Additionally, a large-format pouch cell with designed capacity of 5.4 Ah was assembled (Supplementary Fig. 29 and Supplementary Table 4). According to its practical discharge capacity and total weight, its specific energy reaches 451 Wh kg⁻¹ (Fig. 4c–e), which is comparable to that of state-of-the-art Li metal batteries using liquid electrolytes.

Electrode-electrolyte interface stability

Li symmetric cells were assembled to study the stability of the WSGPE against Li metal. The voltage-time curve of Li|WSGPE|Li cell shows that the overpotential is only approximately 200 mV without soft short-circuit when the current density is increased even to 1 mA cm⁻² (Fig. 5a). This indicates that the WSGPE can effectively inhibit Li dendrites³⁶. Under a current density of 0.5 mA cm⁻² and an area capacity of 0.5 mAh cm⁻², a stable plating/stripping process could maintain at least 1500 h with a unilateral overpotential as small as 60 mV (Fig. 5b).

The interfacial impedance of the cell is decreased and stabilized with cycling (Supplementary Fig. 30). After 100 cycles, the interfacial

impedances of the cell are stabilized at about 120 Ω , indicating the formation of a stable high conductivity SEI layer. However, liquid electrolyte, FEP-free GPE and PTFMA-free GPE cells are short-circuited at 166 h, 293 h and 236 h, respectively (Supplementary Fig. 31a–c). During cycling, the interfacial impedances of the three control samples show a tendency to decrease firstly and then increase before short circuit (Supplementary Fig. 31d–f). That means the generated SEI layer is unstable and cannot effectively inhibit the decomposition of the electrolyte on the Li surface in the control samples.

The morphologies of deposited Li metals were investigated by scanning electron microscope (SEM). As shown in Supplementary Fig. 32a, even after long-term cycling, the Li surface of the Li|WSGPE|Li cell remains overall dense and smooth, without pores and Li dendrites. As a contrast, the surfaces of Li metals from liquid electrolyte, FEP-free GPE and PTFMA-free GPE cells show obvious dendritic morphologies (Supplementary Fig. 32b–d), coincidence with the short-circuit and severe capacity fading^{37,38}.

In-depth X-ray photoelectron spectroscopy (XPS) was used to analyze the composition of SEI in WSGPE system. The weak solvation structure in WSGPE would lead to the preferential decomposition of TFSI[−] anions³⁹. High content of high-strength LiF (685.1 eV in F 1s spectrum) and fast Li⁺ conductor Li₃N (398.1 eV in the N 1s spectrum) are found in inner SEI, while the outer is rich in organic species, including C–C/C–H, C–O, C=O and RO–Li (Fig. 5c–e and Supplementary Fig. 33a)^{24,40,41}. Additionally, from O 1s spectrum, the content of Li₂O (528.6 eV) is significantly increased in the inner SEI (Fig. 5f)⁴⁰, which is beneficial to avoiding severe side reactions and inhibiting Li dendrites^{40–42}. S species with higher oxidation states (SO₃^{2−}/–SO₂–) are located in the outer layer of SEI, while more Li₂S can be detected near Li (Supplementary Fig. 33b). The complete decomposition product of TFSI[−], Li₂S, can improve the passivation ability of SEI effectively⁴³.

Furthermore, the homogeneity of SEI in WSGPE battery was investigated by time-of flight secondary ion mass spectrometry (TOF–SIMS). As shown in Fig. 5g, h and Supplementary Fig. 34, high content of LiF is uniformly distributed on the surface and in the inner part of SEI, while the Li₂CO₃ produced by solvent decomposition in the inner part is negligible. In summary, the double dipole coupling bonds induced weak solvation structure promotes the formation of LiF-rich SEI during cycling, and this interfacial composition reduces the diffusion energy barriers at the Li–electrolyte interface and promotes the migration of Li⁺ through the SEI deposited in a parallel manner instead of dendritic Li deposition (Fig. 5i).

To further evaluate the stability of the WSGPE against high-voltage positive electrodes, the surface morphology and phase evolution of NCM811 after cycling (100 cycles at 188 mA g^{−1}) were characterized by high resolution transmission electron microscopy (HRTEM) and X-ray diffraction (XRD). As shown in Fig. 6a, a dense and uniform thin cathode electrolyte interphase (CEI) with thickness of 3 nm is formed on the cycled NCM811 in WSGPE battery. The uniform and thin CEI not only reduces the polarization during the cycling, but also restrains the structure transition of NCM811. In stark contrast, the CEI of NCM811 from liquid cell is unevenly distributed (Fig. 6b), which causes the battery capacity decline^{44,45}. It has been reported that the evolution of the (003) peak can reflect the changes in the crystal volume of NCM811. The (003) peak of NCM811 cycled in the liquid electrolyte shifted to a lower angle, indicating irreversible structural changes of NCM811. In contrast, the (003) peak of NCM811 cycled in WSGPE remains almost constant, suggesting good structural reversibility and integrity (Supplementary Fig. 35).

The composition of CEI in WSGPE batteries was further analyzed by in-depth XPS. With the increase of the sputtering time, the contents of organic species gradually decrease, while the contents of LiF (F 1s spectrum) and Li₂O (O 1s spectrum) significantly increase (Fig. 6c, d)^{24,46,47}. LiF is well known for its electronic insulation nature,

thus LiF can stop electron tunneling through CEI, further prevent side reactions^{48–50}. The inner Li₂O, meanwhile, ensures the uniform Li⁺ transport and enhances the mechanical strength of CEI^{51,52}. Moreover, the obvious –CF₃ peak in C 1s spectrum indicates that there is a large amount of PTFMA residue on the NCM811 surface (Fig. 6e). The –CF₃ group in PTFMA has strong electron-withdrawing ability, which strengthen the coordination of TFSI[−] to Li⁺. As precursor of passivation layer, more Li⁺–TFSI[−] ligands trigger anion-derived interfacial chemistry at the electrode surface, providing more F sources to generate LiF (Fig. 6f)⁴¹. Therefore, WSGPE can form uniform EELs enriched with LiF and Li₂O, enabling long-term and stable cycling of high-voltage Li metal batteries at extreme temperatures.

Discussion

Supplementary Fig. 36 and Supplementary Table 5 provide a comparison on operation temperature ranges with different electrolytes. Traditional liquid electrolytes have good performance at LT, but often fail at HT due to low solvent boiling points. Solid polymer electrolytes (SPEs) usually deliver good HT performance, but are difficult to work below freezing temperatures caused by limited ionic conductivities. Gel polymer electrolytes (GPEs) can work below RT, but at extreme temperatures, solvation structures in the electrolytes have a significant impact on their performance. The WSGPE obtained by rational interaction design, has a wide temperature operation range from −30~80 °C, which is well suited for practical applications.

Additionally, the performance of different electrolyte systems is compared in Supplementary Fig. 36b. The WSGPE combines the advantages of conventional LHCEs and GPEs, and in addition to ionic conductivity, it has more attractive features than commercial liquid electrolytes, including high electrode compatibility, a wide electrochemical window, thorough non-flammability, no-leakage, and wide-temperature performance. Therefore, the WSGPE can obtain high-voltage Li metal batteries with high safety and wide-temperature operation, while realizing high specific energy.

In summary, a bioinspired weakly-solvated gel polymer electrolyte was successfully developed by double dipole coupling. The in situ polymerized polymer PTFMA interacts with FEP through asymmetric double dipole coupling bonds, effectively pulling solvate molecules out of the first Li⁺ solvation sheath to form a weak solvation structure. More surprisingly, the weak solvation structure promotes charge transfer at the interface under LT and induces the formation of wide-temperature stable high-performance EELs. As a result, the all-fluorinated WSGPE promotes the formation of LiF-rich EELs to stabilize the Li metal and the high-voltage positive electrode. The Li|WSGPE|NCM811 cell can operate in a wide temperature range from −30 to 80 °C. The Li||NCM811 pouch cell can deliver a high specific energy of 490.8 Wh kg^{−1}. This work introduces a concept that modulates the coordination structure and regulates the interfacial chemistry in GPEs, which would be a practical method to develop high-performance Li metal batteries under extreme temperatures.

Methods

Preparation of WSGPE

Lithium bis(trifluoromethanesulfonyl)imide (LiTFSI, 99.9%, Canrd New Energy Technology), ethyl 3,3,3-trifluoropropanoate (FEP, 98%, Aladdin), fluoroethylene carbonate (FEC, 99.95%, Canrd New Energy Technology), 2,2,2-trifluoroethyl methacrylate (TFMA, ≥98%, Aladdin) and poly(ethylene glycol) diacrylate (PEGDA, Sigma-Aldrich, *M_n* = 575) were used as received. The following processes were performed in an argon-filled glovebox (M. Braun). To prepare the WSGPE, 5 wt.% FEC additive, 20 wt.% TFMA monomer, 1 wt.% PEGDA crosslinker and 0.5 wt.% 2,2′-Azobis(2-methylpropionitrile) (AIBN, ≥99%, Aladdin) initiator were co-dissolved in 1 M LiTFSI-FEP as precursor. After that, the precursor was cured at 70 °C for 5 h.

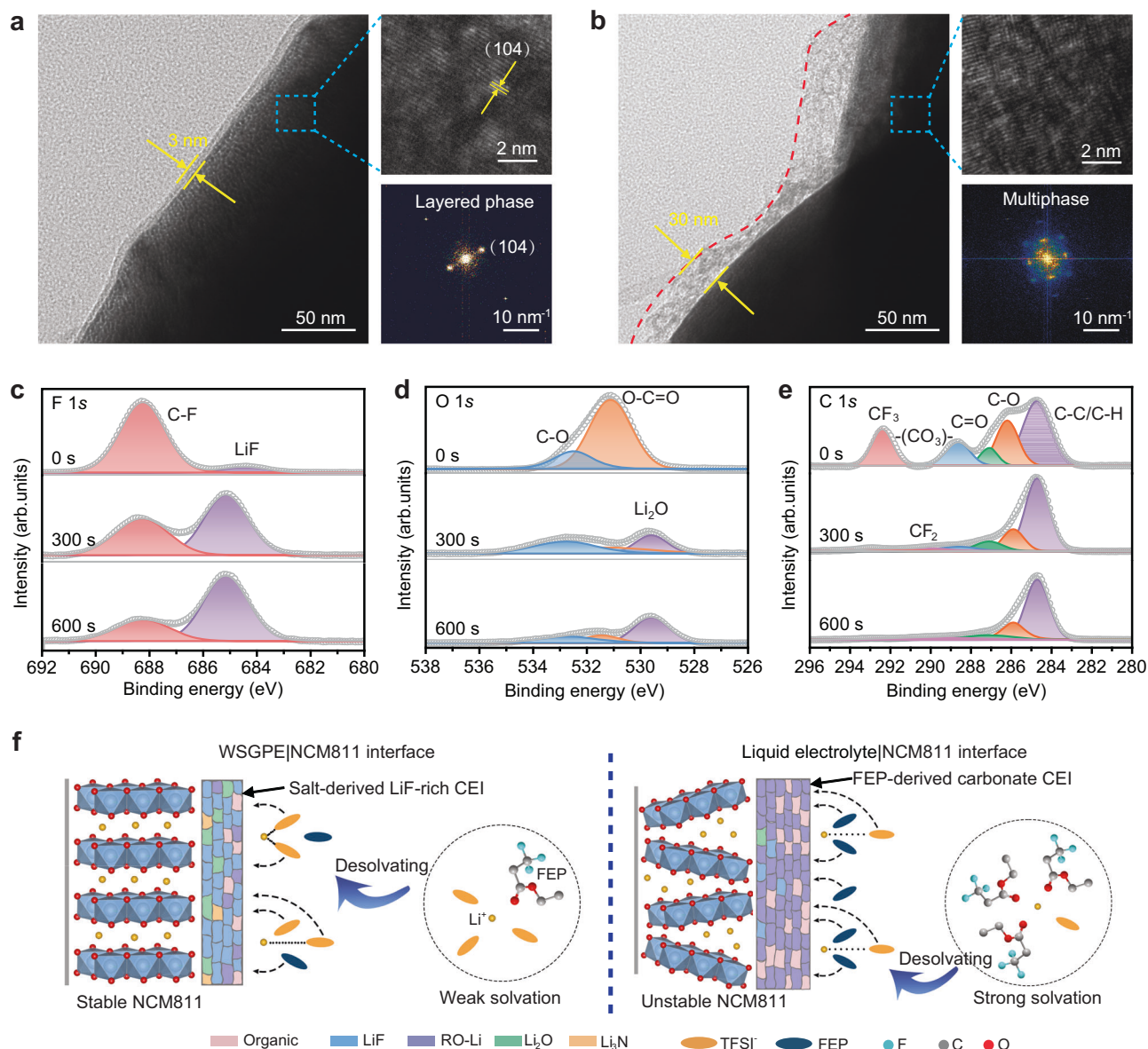


Fig. 6 | NCM811-electrolyte interface characterizations. HRTEM analyses of the cycled NCM811 (100 cycles at 188 mA g^{-1}) using WSGPE (a) and liquid electrolyte (b). XPS spectra of NCM811 after 100 cycles at 188 mA g^{-1} : F 1s (c), O 1s (d) and C 1s

(e). **f** Schematic illustration of NCM811-electrolyte interface of Li|WSGPE | NCM811 and Li|liquid electrolyte|NCM811 batteries. Source data are provided as a Source Data file.

Characterization of WSGPE

Fourier transform infrared (FTIR) spectra of electrolytes were collected on a Thermo Scientific Nicolet 6700 instrument. Raman spectra were collected on a Via Renishaw Raman spectrometer system using a 532 nm wavelength laser. The precursor solution and polymer electrolyte were dissolved in Chloroform- d_1 for NMR analysis on a Bruker AVANCE III 600 MHz. Flame-retardant properties were tested by combustion experiment.

The electrochemical measurements and battery testing were carried out in an environmental chamber. The ionic conductivities of the electrolyte samples were measured by electrochemical impedance spectroscopy (EIS). The cells were assembled using two stainless steel (SS) blocking electrodes and tested on a CHI 660E electrochemical workstation (CH Instruments). A potentiostatic signal with an amplitude of 5 mV was applied over a frequency range of 0.1– 10^6 Hz. The system was allowed to equilibrate at open-circuit voltage for 1 min before beginning the EIS measurements. The data acquisition was set to collect 12 points per decade of frequency. The

cells were kept in the oven for at least 2 h at each temperature point (from -40 to 80°C) for the conductivity measurements. The Li||SS cells were assembled to conduct linear sweep voltammetry (LSV) tests at 25°C to measure the electrochemical window by using a VMP3 multichannel electrochemical workstation (Bio Logic Science Instruments). The LSV curves were examined from 0 to 6 V at a scan rate of 0.1 mV s^{-1} . The oxidation current density was set as $10 \mu\text{A cm}^{-2}$ and the potential values were recorded. The lithium-ion transference number (t_{Li^+}) was determined via Li symmetric cells by EIS testing and direct current (DC) polarization. t_{Li^+} is calculated by the following formula:

$$t_{\text{Li}^+} = \frac{I_s(\Delta V - I_0 R_0)}{I_0(\Delta V - I_s R_s)} \quad (1)$$

where I_s and I_0 represent the steady-state and initial currents, respectively; R_0 and R_s represent the interface resistances before and after polarization, respectively.

Battery assembly and characterization

NCM811 were prepared by a slurry-coating method. A slurry mixture consisting of 80 wt.% NCM811 active material (MTI), 10 wt.% polyvinylidene fluoride (PVDF, Aladdin, $M_w = 110,000$) binder and 10 wt.% conductive carbon black (SP, MTI) in *N*-methyl pyrrolidone (NMP, 99.9%, Canrd) was coated on aluminum foil (15 μm thick) and then vacuum dried at 110 °C for 12 h. LCO were prepared by the same method. Coin cells (CR2025 type) were assembled in an argon-filled glovebox using Celgard 2400 separator (PP, 25 μm thick, 41% porosity, Canrd) and Li negative electrodes (diameter: 15.6 mm, thickness: 0.45 mm, MTI). Precursor solution was injected into the separator (60 μL) and then the coin cells were sealed. After standing for 2 h, the coin cells were cured in an oven (70 °C for 5 h). The pouch cells were fabricated in a glovebox. After aged at 70 °C for 12 h, the pouch cells were activated by one initial cycle, followed by a degassed process. During cycling, the pouch cells were sandwiched in the stainless-steel clamping device with an external pressure of approximately 196 kPa.

Galvanostatic rate measurements were carried out from 0.1 to 1 mA cm^{-2} by using Li symmetric cells which cycled 10 times at each current density. Long-term galvanostatic cycling was performed at 0.5 mA cm^{-2} with a cut-off capacity of 0.5 mAh cm^{-2} . Tafel plot was obtained from LSV measurement using Li symmetrical cells at a scan rate of 1 mV s^{-1} . The values of exchange current density were calculated using the Tafel equation:

$$\eta = a + b \log I \quad (2)$$

where η and I are the potential and current, respectively, and a and b are constants that could be acquired after fitting the data.

The rate and cycling performances of Li||NCM811 and Li||LCO cells were executed on a battery test system (LAND CT 2001A). The cycled cells were carefully disassembled in a glovebox, and the cycled Li foils and NCM811 positive electrodes were washed with dimethyl carbonate (DMC, 99%, Aladdin) and dried at 25 °C. The morphologies of Li were observed by scanning electron microscope (SEM, Hitachi S-4800). X-ray photoelectron spectroscopy (XPS) was performed on Thermo Scientific K-Alpha. All peaks were fitted according to the reference peak of C-C bond at 284.8 eV. X-ray diffraction (XRD) was performed on the X-ray diffractometry (Rigaku Smartlab). A filtered Cu K α 1 ($\lambda = 0.15406 \text{ nm}$) radiation source at 40 kV and 40 mA was used. XRD data were collected at 25 °C in the range of 10°–80°. Time-of-flight secondary ion mass spectrometry (TOF-SIMS) was carried out on a TOF-SIMS 5–100 instrument (ION-TOF GmbH) equipped with Bi³⁺ as the primary ion source (30 keV) over an area of 250 $\mu\text{m} \times 250 \mu\text{m}$. The depth profiles of TOF-SIMS were acquired on the area of 70 $\mu\text{m} \times 70 \mu\text{m}$ using Cs⁺ as the sputter source (2 keV), and the sputter rate is about 10 nm min^{-1} on SiO₂. For the high-resolution transmission electron microscopy (HRTEM, JEM-2100F) tests, the positive electrodes were extracted from the cycled Li||NCM811 cells and thoroughly cleaned with DMC. The extracted powder was ultrasonically dispersed in ethanol (Aladdin) and then deposited on a copper grid for TEM observation. The samples were exposed to air for no more than 5 s. Crystal structure images were generated using the VESTA software package³³.

Simulation details

The molecular dynamic simulations were conducted for an electrolyte system containing 50 PTfMA, 680 FEC, 2325 FEP, 485 Li⁺, and 485 TFSI[−] species with Gromacs (version 2020.6) software⁵⁴, by adopting the OPLS-AA force field and CM5 atomic charge^{55,56}. The initial simulation box was built by randomly distributed species that were fully relaxed at the B3LYP/6-31 G(d) level considering D3BJ dispersion correction by a Gaussian 16 software⁵⁷, followed by energy minimization and then 0.5 ns NVT (canonical ensemble) simulation. The NPT (isothermal-isobaric ensemble) simulation was performed for 30 ns, in which the

latter 15 ns trajectory was used for final analysis. During simulations the timestep was set as 0.5 fs, and the leap-frog algorithm was used to integrate the Newton's equation of motion. The temperature was maintained at 25 °C using the stochastic velocity rescaling algorithm with a coupling time of 0.1 ps⁵⁸. The Parrinello-Rahman algorithm with a coupling time of 0.5 ps was used to maintain the pressure at 1 atm. The electrostatics was handled with the fast smooth Particle-Mesh Ewald method. The direct space part was cutoff at 1.2 nm, and the reciprocal part was performed with Fast Fourier Transformations using a grid spacing of 0.12 nm and a cubic interpolation. A cut-off of 1.2 nm was used in the Van der Waals interaction.

Data availability

The authors declare that all experimental data and relevant analysis of this work are available from the corresponding author upon request. Source data are provided with this paper.

References

- Feng, Y. et al. Challenges and advances in wide-temperature rechargeable lithium batteries. *Energy Environ. Sci.* **15**, 1711–1759 (2022).
- Nie, Q. et al. Research progress of liquid electrolytes for lithium metal batteries at high temperatures. *Small* **19**, 2302690 (2023).
- Zhang, X. et al. Novel PEO-based composite electrolyte for low-temperature all-solid-state lithium metal batteries enabled by interfacial cation-assistance. *Energy Storage Mater.* **56**, 121–131 (2023).
- Wang, H. et al. A novel hyperbranched polyurethane solid electrolyte for room temperature ultra-long cycling lithium-ion batteries. *Energy Storage Mater.* **66**, 103188 (2024).
- Gou, J. et al. An ultrahigh modulus gel electrolytes reforming the growing pattern of Li dendrites for interfacially stable lithium-metal batteries. *Adv. Mater.* **36**, 2309677 (2024).
- Xue, J. X. et al. In situ forming gel polymer electrolyte for high energy-density lithium metal batteries. *Small* **20**, 2307553 (2024).
- Yang, B. et al. High-safety lithium metal pouch cells for extreme abuse conditions by implementing flame-retardant perfluorinated gel polymer electrolytes. *Energy Storage Mater.* **65**, 103124 (2024).
- Luo, D. et al. Electrolyte design for lithium metal anode-based batteries toward extreme temperature application. *Adv. Sci.* **8**, 2101051 (2021).
- Liu, Q. & Wang, L. Fundamentals of electrolyte design for wide-temperature lithium metal batteries. *Adv. Energy Mater.* **13**, 2301742 (2023).
- Lu, Y. et al. Tuning the Li⁺ solvation structure by a “bulky coordinating” strategy enables nonflammable electrolyte for ultrahigh voltage lithium metal batteries. *ACS Nano* **17**, 9586–9599 (2023).
- Zou, Y. et al. High performance low-temperature lithium metal batteries enabled by tailored electrolyte solvation structure. *Small* **19**, 2203394 (2023).
- Mao, M. et al. Anion-enrichment interface enables high-voltage anode-free lithium metal batteries. *Nat. Commun.* **14**, 1082 (2023).
- Liu, Y. et al. Regulating electrolyte solvation structures via diluent-solvent interactions for safe high-voltage lithium metal batteries. *Small* **20**, 2311812 (2024).
- Zhang, J. et al. Weakly solvating cyclic ether electrolyte for high-voltage lithium metal batteries. *ACS Energy Lett.* **8**, 1752–1761 (2023).
- Wang, F. et al. Fluorinated nonflammable in situ gel polymer electrolyte for high-voltage lithium metal batteries. *ACS Appl. Mater. Interfaces* **15**, 39265–39275 (2023).
- Lin, Z. et al. Regulating solvation structure in gel polymer electrolytes with covalent organic frameworks for lithium metal batteries. *Energy Storage Mater.* **53**, 917–926 (2022).
- Huang, K. et al. Optimizing Li-ion solvation in gel polymer electrolytes to stabilize Li-metal anode. *ChemSusChem* **16**, e202300671 (2023).

18. Guo, C. et al. Multifunctional nitrile additives for inducing pseudo-concentration gel-polymer electrolyte: Enabling stable high-voltage lithium metal batteries. *Energy Storage Mater.* **71**, 103683 (2024).
19. Maberly, S. C. & Gontero, B. *The Leaf: A Platform for Performing Photosynthesis* (Springer Cham, 2018).
20. Liu, Y. et al. Recent development in topological polymer electrolytes for rechargeable lithium batteries. *Adv. Sci.* **10**, 2206978 (2023).
21. Nakano, Y., Shinke, K., Ueno, K. & Tsutsumi, H. Gel polymer electrolytes based on poly (methacrylamide) derivative having branched pendant with terminal nitrile groups. *Solid State Ion* **293**, 13–17 (2016).
22. Jia, D. et al. Multifunctional polymer bottlebrush-based gel polymer electrolytes for lithium metal batteries. *Mater. Today Nano.* **15**, 100128 (2021).
23. Li, H., Feng, T., Gao, J. & Wu, M. In situ construction of 3D cross-linked gel polymer electrolyte toward high performance and safety lithium metal batteries. *J. Power Sour.* **618**, 235189 (2024).
24. Wang, Q. et al. Molecular reactivity and interface stability modification in in-situ gel electrolyte for high performance quasi-solid-state lithium metal batteries. *Energy Environ. Mater.* **6**, e12351 (2023).
25. Zhang, C. et al. Nonflammable, localized high-concentration electrolyte towards a high-safety lithium metal battery. *Energy Storage Mater.* **52**, 355–364 (2022).
26. He, R. et al. Active diluent-anion synergy strategy regulating non-flammable electrolytes for high-efficiency Li metal batteries. *Angew. Chem. Int. Ed.* **63**, e202317176 (2024).
27. Ma, M. et al. Designing weakly solvating solid main-chain fluoropolymer electrolytes: synergistically enhancing stability toward Li anodes and high-voltage cathodes. *ACS Energy Lett.* **6**, 4255–4264 (2021).
28. Hu, L. et al. Restructuring electrolyte solvation by a versatile diluent toward beyond 99.9% coulombic efficiency of sodium plating/stripping at ultralow temperatures. *Adv. Mater.* **36**, 2312161 (2024).
29. Li, Q. et al. Low-temperature electrolyte design for lithium-ion batteries: prospect and challenges. *Chem-Eur. J.* **27**, 15842–15865 (2021).
30. Jia, M. et al. Fluorinated bifunctional solid polymer electrolyte synthesized under visible light for stable lithium deposition and dendrite-free all-solid-state batteries. *Adv. Funct. Mater.* **31**, 2101736 (2021).
31. Lin, W. et al. Weak-coordination electrolyte enabling fast Li⁺ transport in lithium metal batteries at ultra-low temperature. *Small* **19**, 2207093 (2023).
32. Zhou, X., Huang, J., Pan, Z. & Ouyang, M. Impedance characterization of lithium-ion batteries aging under high-temperature cycling: Importance of electrolyte-phase diffusion. *J. Power Sour.* **426**, 216–222 (2019).
33. Chen, Y. et al. Breaking solvation dominance of ethylene carbonate via molecular charge engineering enables lower temperature battery. *Nat. Commun.* **14**, 8326 (2023).
34. Liu, J., Li, X., Huang, J., Yang, G. & Ma, J. Additive-guided solvation-regulated flame-retardant electrolyte enables high-voltage lithium metal batteries with robust electrode electrolyte interphases. *Adv. Funct. Mater.* **34**, 2312762 (2024).
35. Xie, Y. et al. A novel flame-retardant nitrile-based gel polymer electrolyte for quasi-solid-state lithium metal batteries. *Coll. Surf. A* **670**, 131487 (2023).
36. Lu, Y. et al. Critical current density in solid-state lithium metal batteries: mechanism, influences, and strategies. *Adv. Funct. Mater.* **31**, 2009925 (2021).
37. Yang, S. et al. A supertough, nonflammable, biomimetic gel with neuron-like nanoskeleton for puncture-tolerant safe lithium metal batteries. *Adv. Funct. Mater.* **33**, 2304727 (2023).
38. Zhang, C. et al. Highly oxidation-resistant ether gel electrolytes for 4.7 V high-safety lithium metal batteries. *Adv. Energy Mater.* **13**, 2203870 (2023).
39. Zhang, G. et al. A monofluoride ether-based electrolyte solution for fast-charging and low-temperature non-aqueous lithium metal batteries. *Nat. Commun.* **14**, 1081 (2023).
40. Hu, J. et al. Dual fluorination of polymer electrolyte and conversion-type cathode for high-capacity all-solid-state lithium metal batteries. *Nat. Commun.* **13**, 7914 (2022).
41. Zhang, W., Yang, T., Liao, X., Song, Y. & Zhao, Y. All-fluorinated electrolyte directly tuned Li⁺ solvation sheath enabling high-quality passivated interfaces for robust Li metal battery under high voltage operation. *Energy Storage Mater.* **57**, 249–259 (2023).
42. Kim, M. S. et al. Suspension electrolyte with modified Li⁺ solvation environment for lithium metal batteries. *Nat. Mater.* **21**, 445–454 (2022).
43. Li, T. et al. Stable anion-derived solid electrolyte interphase in lithium metal batteries. *Angew. Chem. Int. Ed.* **60**, 22683–22687 (2021).
44. Zhang, L. et al. Practical 4.4 V Li||NCM811 batteries enabled by a thermal stable and HF free carbonate-based electrolyte. *Nano Energy* **96**, 107122 (2022).
45. Li, G. et al. Achieving a highly stable electrode/electrolyte interface for a nickel-rich cathode via an additive-containing gel polymer electrolyte. *ACS Appl. Mater. Interfaces* **14**, 36656–36667 (2022).
46. Zhu, T. et al. Constructing flame-retardant gel polymer electrolytes via multiscale free radical annihilating agents for Ni-rich lithium batteries. *Energy Storage Mater.* **50**, 495–504 (2022).
47. Chen, Y. et al. Engineering an insoluble cathode electrolyte interphase enabling high performance NCM811/graphite pouch cell at 60 °C. *Adv. Energy Mater.* **12**, 2201631 (2022).
48. Tan, J., Matz, J., Dong, P., Shen, J. & Ye, M. A growing appreciation for the role of LiF in the solid electrolyte interphase. *Adv. Energy Mater.* **11**, 2100046 (2021).
49. Liu, J. et al. Amide-functional, Li₃N/LiF-rich heterostructured electrode electrolyte interphases for 4.6 V Li||LiCoO₂ batteries. *Adv. Energy Mater.* **13**, 2300084 (2023).
50. Yang, Y., Wang, H., Zhu, C. & Ma, J. Armor-like inorganic-rich cathode electrolyte interphase enabled by penta-fluorophenylboronic acid for high-voltage Li||NCM622 batteries. *Angew. Chem. Int. Ed.* **62**, e202300057 (2023).
51. Zhang, J. et al. Construction of stable Li₂O-rich solid electrolyte interphase for practical PEO-based Li-metal batteries. *Adv. Energy Mater.* **14**, 2302587 (2024).
52. Shi, J. et al. High-rate and durable sulfide-based all-solid-state lithium battery with in situ Li₂O buffering. *Energy Storage Mater.* **51**, 306–316 (2022).
53. Momma, K. & Izumi, F. Vesta 3 for three-dimensional visualization of crystal, volumetric and morphology data. *J. Appl. Crystallogr.* **44**, 1272–1276 (2011).
54. Van Der Spoel, D. et al. GROMACS: Fast, flexible, and free. *J. Comput. Chem.* **26**, 1701–1718 (2005).
55. Damm, W., Frontera, A., Tirado-Rives, J. & Jorgensen, W. L. OPLS all-atom force field for carbohydrates. *J. Comput. Chem.* **18**, 1955–1970 (1997).
56. Marenich, A. V., Jerome, S. V., Cramer, C. J. & Truhlar, D. G. Charge Model 5: an extension of Hirshfeld population analysis for the accurate description of molecular interactions in gaseous and condensed phases. *J. Chem. Theory Comput.* **8**, 527–541 (2012).
57. Tirado-Rives, J. & Jorgensen, W. L. Performance of B3LYP density functional methods for a large set of organic molecules. *J. Chem. Theory Comput.* **4**, 297–306 (2008).
58. Bussi, G., Donadio, D. & Parrinello, M. Canonical sampling through velocity-rescaling. *J. Chem. Phys.* **126**, 014101 (2007).

Acknowledgements

This study was supported by the National Natural Science Foundation of China under Grant No. 52472103 (S.Z.). We also thank the support from Instrumental Analysis Center at SJTU.

Author contributions

S.L. conceived the idea and performed the experiments. S.Z., H.P. and C.Y. supervised the project. S.C. and X.H. performed DFT calculations and MD simulations. S.L., Z.W. and J.S. measured SEM, TEM and XPS. W.T. assembled pouch cells and performed measurements. S.L., H.Q., H.P., X.K. and S.Z. wrote the manuscript. All of the authors commented on the manuscript.

Competing interests

The authors declare no competing interests.

Additional information

Supplementary information The online version contains supplementary material available at <https://doi.org/10.1038/s41467-025-57856-w>.

Correspondence and requests for materials should be addressed to Hui Pan, Cheng Yang, Xiujun Han or Shenmin Zhu.

Peer review information *Nature Communications* thanks Huijun Yang, and the other, anonymous, reviewer(s) for their contribution to the peer review of this work. A peer review file is available.

Reprints and permissions information is available at <http://www.nature.com/reprints>

Publisher's note Springer Nature remains neutral with regard to jurisdictional claims in published maps and institutional affiliations.

Open Access This article is licensed under a Creative Commons Attribution-NonCommercial-NoDerivatives 4.0 International License, which permits any non-commercial use, sharing, distribution and reproduction in any medium or format, as long as you give appropriate credit to the original author(s) and the source, provide a link to the Creative Commons licence, and indicate if you modified the licensed material. You do not have permission under this licence to share adapted material derived from this article or parts of it. The images or other third party material in this article are included in the article's Creative Commons licence, unless indicated otherwise in a credit line to the material. If material is not included in the article's Creative Commons licence and your intended use is not permitted by statutory regulation or exceeds the permitted use, you will need to obtain permission directly from the copyright holder. To view a copy of this licence, visit <http://creativecommons.org/licenses/by-nc-nd/4.0/>.

© The Author(s) 2025